Topological Flat-Band-Driven Metallic Thermoelectricity

Fabian Garmroudi,[1,2,*] Jennifer Coulter,[3,†] Illia Serhiienko,[4,5] Simone Di Cataldo,[1,6] Michael Parzer,[1] Alexander Riss,[1] Matthias Grasser,[1] Simon Stockinger,[1] Sergii Khmelevskyi,[7] Kacper Pryga,[8] Bartlomiej Wiendlocha,[8] Karsten Held,[1] Takao Mori,[4,5] Ernst Bauer,[1] Antoine Georges,[3,9,10,11] and Andrej Pustogow[1,‡]

[1]*Institute of Solid State Physics, TU Wien, 1040 Vienna, Austria*
[2]*Materials Physics Applications—Quantum, Los Alamos National Laboratory, Los Alamos, New Mexico 87545, USA*
[3]*Center for Computational Quantum Physics, Flatiron Institute, New York 10010, USA*
[4]*International Center for Materials Nanoarchitectonics (WPI-MANA), National Institute for Materials Science, Tsukuba 305-0044, Japan*
[5]*University of Tsukuba, Tsukuba 305-8577, Japan*
[6]*Dipartimento di Fisica, Sapienza University of Rome, Piazzale Aldo Moro 5, 00185 Roma, Italy*
[7]*Vienna Scientific Cluster Research Center, TU Wien, 1040 Vienna, Austria*
[8]*AGH University of Krakow, Faculty of Physics and Applied Computer Science, Aleja Mickiewicza 30, 30-059 Krakow, Poland*
[9]*Collège de France, PSL University, 75005 Paris, France*
[10]*Department of Quantum Matter Physics, University of Geneva, 1211 Geneva, Switzerland*
[11]*Centre de Physique Théorique, Ecole Polytechnique, 91128 Palaiseau, France*

(Received 12 April 2024; revised 13 January 2025; accepted 18 April 2025; published 14 May 2025)

Materials where flattened electronic dispersions arise from destructive phase interference, rather than localized orbitals, have emerged as promising platforms for studying emergent quantum phenomena. Crucial next steps involve tuning such flat bands to the Fermi level, where they can be studied at low energy scales, and assessing their potential for practical applications. Here, we show that the interplay of highly dispersive and ultraflat bands inherent to these systems can lead to extreme interband scattering-induced electron-hole asymmetry, which can be harnessed in thermoelectrics. Our comprehensive theoretical and experimental investigation of $Ni_3In_{1-x}Sn_x$ kagome metals supports this concept, showing that it could lead to thermoelectric performance on par with state-of-the-art semiconductors such as Bi_2Te_3. In Ni_3In, scattering-induced electron-hole asymmetry is, however, subdued by an exotic conduction mechanism arising from quantum tunneling of charge carriers between Dirac bands, unrelated to the flat band itself. We outline strategies to selectively switch off this tunneling transport through negative chemical pressure or strain. Our study proposes a new direction to explore in topological flat-band systems and vice versa introduces a novel tuning knob for thermoelectric materials.

DOI: 10.1103/PhysRevX.15.021054 Subject Areas: Condensed Matter Physics

I. INTRODUCTION

Topological flat-band (TFB) materials are of immense current interest, as they promise a rich tapestry of emergent correlation phenomena and novel physics to be discovered [1,2]. Certain frustrated geometries such as the dice, Lieb, or kagome lattices are theoretically predicted to support *completely flat* electronic bands, that is, a quasi-infinitely degenerate set of quantum states arising from internal symmetries or local topology [3–5]. For instance, within a single-orbital tight-binding model for the kagome lattice—a corner-sharing network of triangles—destructive interference among electronic hopping pathways leads to perfectly flat bands in two dimensions [Fig. 1(a)]. The pyrochlore lattice, a corner-sharing network of tetrahedra, extends this notion to the third dimension [Fig. 1(b)]. Such lattice-borne TFBs have emerged as promising platforms for designing novel quantum phases of matter on demand, as the electron-electron interaction becomes decisive compared to the quenched kinetic energy [6,7]. While various TFB candidates have been proposed in recent years [8–10],

*Contact author: f.garmroudi@gmx.at
†Contact author: jcoulter@flatironinstitute.org
‡Contact author: pustogow@ifp.tuwien.ac.at

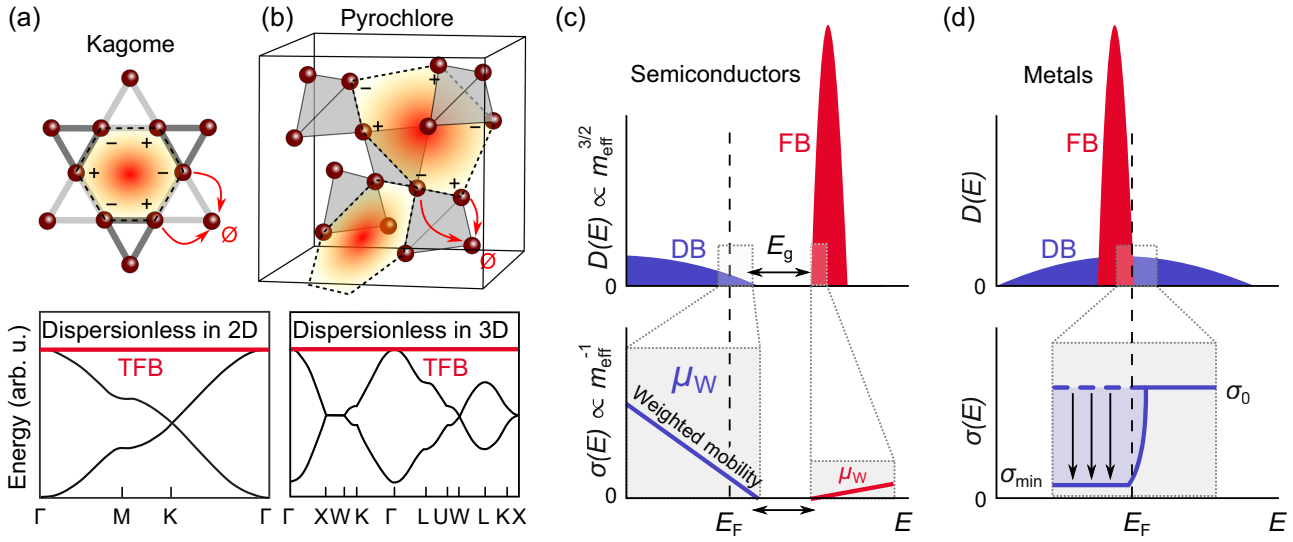

FIG. 1. Topological flat bands for thermoelectric materials design. (a) Frustrated kagome and (b) pyrochlore lattices with compact localized states (red-yellow) arising from destructive interference (Ø) of nearest-neighbor hopping paths. This yields topological flat bands in two and three dimensions, respectively. (c) Energy-dependent density of states $D(E)$ and transport distribution function $\sigma(E)$ for a dispersive and for a flat band, separated by an energy gap. The slope of $\sigma(E)$, the weighted mobility μ_W, determines the electronic quality of TE semiconductors, in the regime near the band edge, where the single-parabolic band approximation holds [14]. (d) $D(E)$ and $\sigma(E)$ for a metal, where dispersive (DB) and flat bands (FBs) overlap and interband scattering creates a very steep edge in $\sigma(E)$.

and there are now even catalogs and databases listing thousands of such materials [11,12], an outstanding challenge and crucial question is how TFBs manifest in the physical properties of the hosting materials and whether their unique electronic structures can be harnessed for practical applications [13].

Here, we recognize the remarkable prospect of TFBs—given that they can be properly tuned around the Fermi level—for thermoelectric (TE) materials. Thermoelectricity refers to the ability of solids to seamlessly interconvert thermal and electrical energy, which is attractive for various power generation and cooling applications [15]. An efficient TE material requires a large power factor $\mathrm{PF} = S^2\sigma$ (S being the Seebeck coefficient and σ the electrical conductivity) and a low thermal conductivity κ, summarized in the dimensionless figure of merit $zT = S^2\sigma\kappa^{-1}T$, where T is the absolute temperature.

Traditionally, only selected semiconductors have been considered to be viable TEs ever since Ioffe proposed them in the mid-20th century [16]. This preference is rooted in the fact that the band gap in semiconductors inherently separates the contributions of low- and high-energy charge carriers (holes and electrons), prerequisite for achieving large S [17]. However, the rather poor σ of semiconductors, even in their heavily doped forms, results in rather low PF and necessitates the use of materials with ultralow lattice thermal conductivity κ_l. To inhibit heat transport via the lattice, TE semiconductors are usually complex alloys comprising multiple elements and a high degree of structural and chemical bonding intricacy [18]. As a downside, crystallographic and chemical features yielding ultralow κ_l often go hand in hand with poor mechanical and thermal stability, limiting the applicability of these materials [19]. Thus, it is crucial to identify materials that display competitive zT arising from large PF rather than from low κ_l [20]. Unfortunately, electronic tuning is hindered by intrinsic trade-offs between σ and S, despite dedicated efforts in the past aimed at overcoming these challenges [21–23].

A. "The best thermoelectric" revisited

What electronic structure provides the highest TE performance? In their seminal work, Mahan and Sofo attempted to answer this simple yet fundamental question by mathematical derivation, establishing conditions for the best thermoelectric [24]. They found that the energy-dependent conductivity of charge carriers, characterized by a unique transport distribution function $\sigma(E)$, must vary rapidly and ideally be shaped like a delta distribution. In other words, charge carriers should contribute only in an infinitely narrow energy interval. Recent theoretical studies [25–29] suggest that a (rectangular) boxcar-shaped transport function of finite width would be optimal and superior to the delta function. In such a scenario, electronic transport is bounded to a finite energy window with $\sigma(E)$ instantaneously dropping to zero outside that interval. In real materials, however, $\sigma(E)$ neither is bounded to an infinitely narrow energy interval nor displays an infinitely steep edge. Instead, $\sigma(E)$ increases linearly with

a finite slope near the band edge [Fig. 1(c)] and becomes weakly energy dependent in the center of a band. In a single-parabolic band model, $\sigma(E) \sim D(E)v^2(E)\tau(E)$, with $D(E)$ being the density of states, $v(E)$ the velocity, and $\tau(E)$ the relaxation time of charge carriers [17]. In semiconductors, which can often be reasonably well described by a single-parabolic band model, S depends on only the distance of the Fermi level E_F from the band edge and is a direct measure of doping. The electrical conductivity σ and, hence, PF, however, depend on the absolute value of $\sigma(E)$ around E_F. This yields a trade-off, since S decreases as E_F is shifted further into the band whereas σ increases. The slope of $\sigma(E)$, commonly referred to as the weighted mobility μ_W, determines, in the single-parabolic band regime, the electronic quality of a TE material, that is, the highest achievable performance at an optimized position of E_F [14]. Enhancing μ_W is not as straightforward as reducing κ_l. It is often wrongly assumed that a flat band with a steep $D(E)$ would also result in a steep $\sigma(E)$. However, while $D(E) \propto m_{\mathrm{eff}}^{3/2}$, $\sigma(E)$ scales inversely with the effective mass m_{eff}^{-1} due to $v^2(E) \propto m_{\mathrm{eff}}^{-1}$ and $\tau(E) \propto m_{\mathrm{eff}}^{-3/2}$. Hence, charge transport via flat bands with exceptionally steep $D(E)$ cannot be directly exploited. In fact, the best thermoelectric semiconductors, such as Bi_2Te_3 and PbTe, usually display very dispersive bands (DBs) around E_F [30,31]. This inevitably means, however, that semiconducting thermoelectrics with dispersive (broad) bands cannot realize a narrow boxcar-shaped or delta-distribution-shaped transport distribution.

Here, we present a materials design principle in which the exceptionally steep band edge of flat bands can actually be exploited to generate a steep edge in $\sigma(E)$ [Fig. 1(d)]. In metals, where FBs overlap with DBs, carriers from the DB can scatter into the FB, locally suppressing $\sigma(E)$. These interband transitions and, hence, the edge occurring in $\sigma(E)$ are directly determined by $D(E)$ of the FB, as shown later. Through this paradigm, we tuned interband scattering of mobile s-like carriers into more localized Ni-3d states and, this way, realized in binary Ni_xAu_{1-x} alloys the highest PF ever reported in a bulk material above room temperature, $PF = 34\ \mathrm{mW\,m^{-1}\,K^{-2}}$ at 560 K, and the highest zT ever reported for a metal, $zT \approx 0.3$ (0.5) at 300 (1100) K [32]. A similar interband scattering scenario is at work also in certain semimetals like CoSi [33,34]—yielding high $PF \approx 6\ \mathrm{mW\,m^{-1}\,K^{-2}}$ but modest $zT \approx 0.1$—and has theoretically been proposed for others [35]. Recently, Graziosi *et al.* derived materials design criteria for metallic thermoelectrics employing a two-parabolic band model [36], and the potential of extreme band asymmetry has even been recognized for narrow-gap semiconductors and topological semimetals [37–39].

While the malleable and ductile nature of metals makes them especially attractive for designing new and innovative TE device structures, e.g., for flexible and wearable electronics [40,41], in the case of Ni_xAu_{1-x}, the high cost of Au poses constraints for practical use and the obvious question arises whether the TE performance could be improved even further up to $zT \approx 1$ near room temperature, competitive with commercial Bi_2Te_3 systems [18,42]. To achieve such a leap of TE performance, an important issue to address is how to further flatten the bands compared to the situation in binary Ni_xCu_{1-x} and Ni_xAu_{1-x}, where alloying and disorder substantially smear the band edges. We argue that metallic TFB systems appear to be near-perfect candidates in this regard, not only because their dispersion is significantly more flattened by geometrical frustration, but also because their band flatness is topologically robust and immune to alloying and chemical disorder.

Additionally, we discover a quantum tunneling mechanism for charge carriers between dispersive bands, unrelated to the flat band, that needs to be taken into consideration when designing scattering-tuned metallic thermoelectrics. Given the importance of this tunneling mechanism, in particular, for linear band crossings near the Fermi level, which are essential band structure features for realizing an optimal boxcar-shaped transport distribution [28], we stress the crucial need for theoretical work reconsidering what kind of electronic structure produces the best thermoelectric.

II. RESULTS

A. Extreme interband scattering in Ni_3In

We implemented the above described concept in a comprehensive experimental and theoretical investigation of a particular promising candidate: the kagome metal Ni_3In. This system has recently been predicted to feature almost dispersionless TFBs in conjunction with two highly dispersive Dirac-like bands in its electronic structure, exactly at E_F [43]. Figure 2(a) shows the crystal unit cell alongside a top view of the AB stacked kagome layers formed by Ni atoms. The alternating sign pattern of the Ni-3d_{xz} orbital texture results in destructive phase interference among inter- and intralayer hopping paths and spatially localized electronic states around the triangular Ni plaquettes [red shaded area in Fig. 2(a)]. This yields ultraflat bands exactly at E_F as shown in Fig. 2(b). These FBs produce an extremely steep edge in $D(E)$ [Fig. 2(c)], whose position with respect to E_F can be tuned exceptionally well via aliovalent Sn substitution at the In site in $Ni_3In_{1-x}Sn_x$ [Fig. 2(d)]. Since Ni_3Sn exists as an isostructural variant, a full solid solution is possible, as confirmed experimentally [inset in Fig. 2(c)].

For a quantitative comparison, we compare in Fig. 3(a) $D(E)$ of $Ni_3In_{1-x}Sn_x$ with those of binary transition metal alloys like Ni_xCu_{1-x} and Ni_xAu_{1-x}. It is evident that, owing to the hopping frustration-induced flattening of the Ni-3d_{xz} bands, the $D(E)$ edge is much steeper for the former. Because of the rapid variation of $D(E)$, the scattering phase

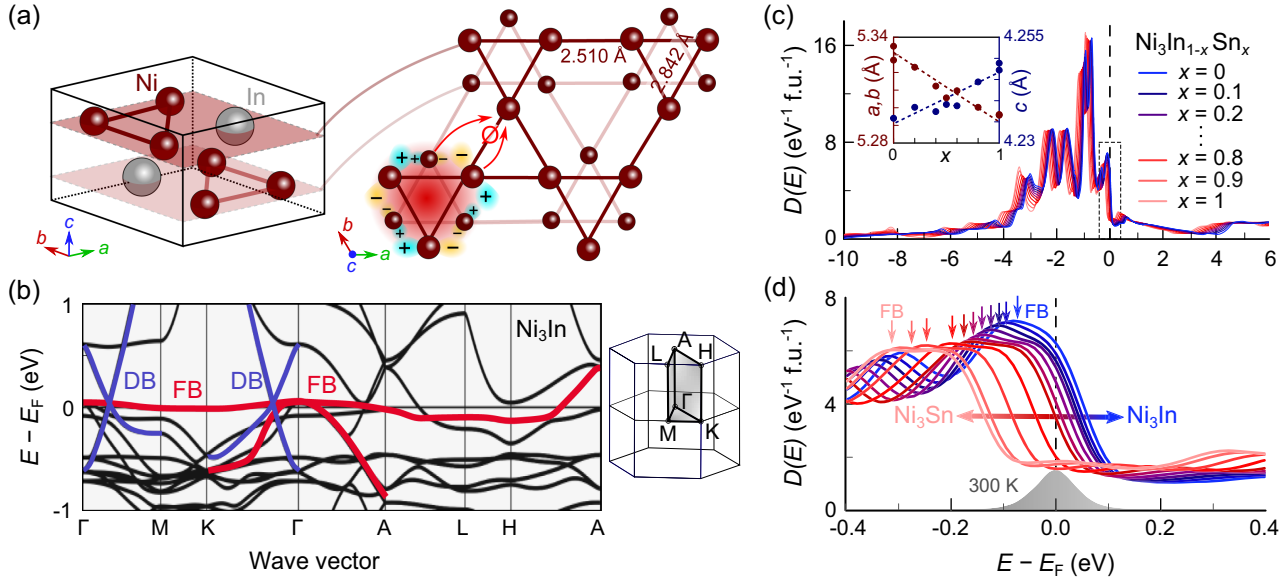

FIG. 2. A kagome system with flat bands at the Fermi level and exceptional tunability. (a) Unit cell of Ni_3In with triangular motifs formed by Ni atoms, showing *AB* stacked breathing kagome lattice planes. Yellow and blue lobes indicate opposite phases of the d_{xz} wave functions, causing destructive interference (Ø) of inter- and intralayer hopping paths (arrows) and localizing electronic states at the triangular plaquettes (red area). (b) Electronic band structure (without spin orbit coupling) of Ni_3In, featuring flat bands (red) and dispersive Dirac-like bands (blue) at the Fermi energy E_F. (c),(d) Alloy-averaged densities of states of $Ni_3In_{1-x}Sn_x$ across various alloy concentrations, showing tunability of the flat band's position relative to E_F via In/Sn substitution. A solid solution is confirmed throughout the entire composition range by x-ray diffraction. Inset: experimental lattice parameters as a function of x at room temperature. The gray shaded area in (d) represents the derivative of the Fermi-Dirac distribution at 300 K, marking the relevant energy range for electronic transport.

space for charge carriers from the underlying DBs exhibits a strong energy dependence as well. By direct application of Fermi's golden rule, it follows that $\tau^{-1}(E) \sim D(E)$. In the following, we refer to it as the $D^{-1}(E)$ model. At this point, we also note that the analytic formula for electron-phonon scattering in deformation potential theory yields $\tau(E) \sim D^{-1}(E)$, which, for parabolic bands, results in the well-known $\tau(E) \sim E^{-1/2}$ dependence of the relaxation time. Figure 3(b) displays $\sigma(E)$, normalized to its values at $E - E_F = 0.2$ eV, to highlight and compare the drop in $\sigma(E)$ around E_F. It can be seen that while in the binary alloys, with mundane Ni-3*d* bands, $\sigma(E)$ reduces to about 50% of its value 0.2 eV above E_F, the kagome metal shows a remarkable drop to less than 10%, while the conductivity remains high at $E > E_F$ in either case. This scattering-induced energy filtering creates pronounced electron-hole asymmetry and results in a very large Seebeck coefficient $S \approx -136\ \mu V\,K^{-1}$ at 300 K, well above those predicted theoretically and achieved experimentally in both Ni_xCu_{1-x} and Ni_xAu_{1-x} [Fig. 3(c)] or any other metal known to date. As shown in Fig. 3(d), the high S coupled with the good metallic nature of $Ni_3In_{1-x}Sn_x$ would result in an outstanding $zT \approx S^2/L \approx 1.1$ at 300 K, rivaling or even surpassing those of today's best semiconductors [42]. We note that $zT \approx S^2/L$ is a very good approximation in highly metallic systems, such as $Ni_3In_{1-x}Sn_x$ and Ni_xAu_{1-x}, especially at high temperatures [32]. Indeed, thermal conductivity measurements (Fig. S1 [44]) confirm that electrons dominate thermal transport and that lattice-driven heat transport is insignificant in $Ni_3In_{1-x}Sn_x$, resulting in $zT = S^2/L$. Thus, only the Seebeck coefficient S and the Lorenz number L determine the performance. Energy filtering of charge carriers right next to either side of E_F enhances electron-hole asymmetry and thereby S. On the other hand, selectively filtering charge carriers at higher energies (approximately $3k_BT$ above E_F) to create a boxcar-shaped transport distribution function $\sigma(E)$ can strongly reduce L relative to the Sommerfeld value, further boosting zT in metallic TEs [45]. Achieving such a scenario via flat-band-induced energy filtering would require different flat bands, one right next to E_F and another slightly above or below E_F, depending on the position of the first, which could be achieved, e.g., by substituting transition metal atoms with localized non-hybridizing impurity bands [46].

The theoretical estimates by the BTE-$D^{-1}(E)$ model, predicting a large Seebeck effect in metallic $Ni_3In_{1-x}Sn_x$, motivated us to experimentally study the TE properties of these compounds. Since large samples are an essential requirement for conducting high-temperature TE measurements, we prepared phase-pure polycrystalline samples in the entire composition range from $x = 0$ to 1 [experimental

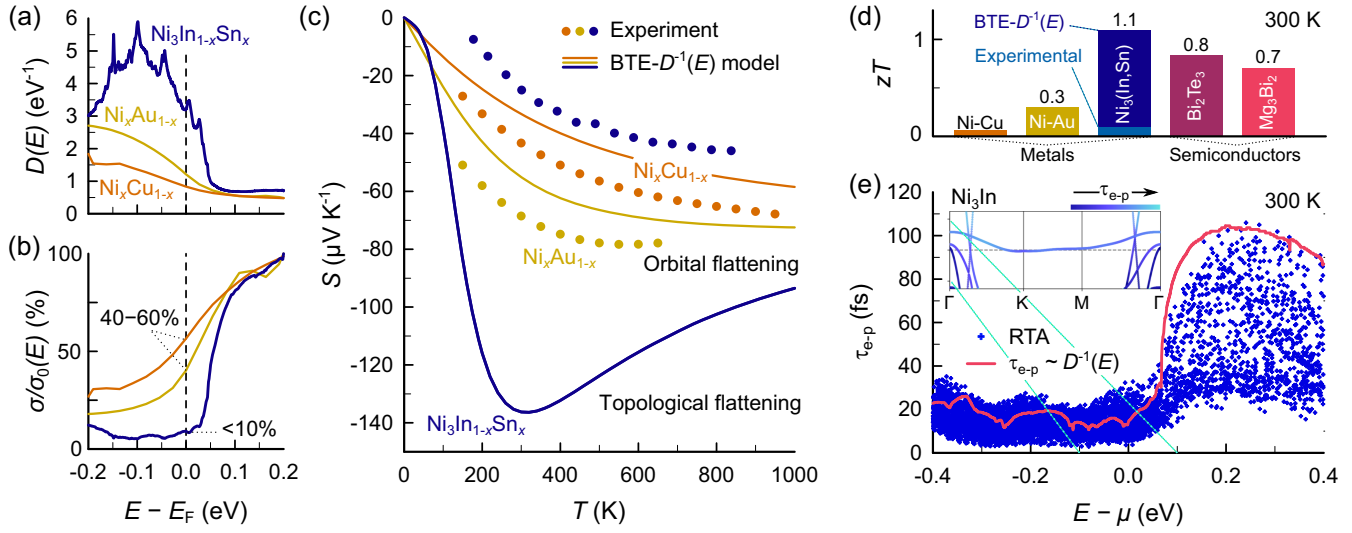

FIG. 3. Comparison to binary transition metal alloys and state-of-the-art semiconductors. (a) Density of states and (b) normalized transport distribution function of $Ni_3In_{1-x}Sn_x$ kagome metals with $x = 0.25$ compared to Ni_xCu_{1-x} and Ni_xAu_{1-x} with $x = 0.4$; calculations were performed within Boltzmann transport theory and using a $D^{-1}(E)$ interband scattering model for the relaxation time [BTE-$D^{-1}(E)$]. (c) Calculated temperature-dependent Seebeck coefficient. A much larger Seebeck coefficient is predicted for $Ni_3In_{1-x}Sn_x$ due to its frustration-enhanced flat bands and scattering phase space. Surprisingly, the experimental $S(T)$ of Ni_3In is significantly lower, raising questions about the accuracy of interband scattering estimates from the $D^{-1}(E)$ model. (d) Comparison of zT at room temperature. An outstanding $zT > 1$ is predicted for $Ni_3In_{1-x}Sn_x$ in the BTE-$D^{-1}(E)$ framework, competitive with the best semiconductors [42]. Here, zT was calculated from $zT \approx S^2/L$, which is a good approximation for these metallic systems due to electronic-dominated heat transport, $\kappa_e = L\sigma T \gg \kappa_l$, at high temperatures (see Fig. S1 [44]). The disagreement with experiments questions the validity of the $D^{-1}(E)$. (e) Carrier lifetimes for electron-phonon scattering from expensive *ab initio* calculations in the relaxation time approximation, however, exhibit good agreement with the $D^{-1}(E)$ model, suggesting that additional mechanisms beyond Boltzmann transport theory influence $S(T)$. Inset: variation of RTA carrier lifetimes in Ni_3In projected onto the band structure around the chemical potential.

lattice parameters in the inset in Fig. 2(c)]. Figure S12 [44] shows $S(T)$ of three representative samples ($x = 0$, 0.5, 1) measured in a very broad temperature range 4–860 K. It can be immediately seen that there is a large disparity between experimental results and theoretical calculations using the BTE-$D^{-1}(E)$ model [see also Fig. 3(c)], which is surprising considering that usually very consistent agreement is obtained, e.g., in binary transition metal alloys [32] or in semimetallic CoSi [47]. It should also be pointed out that, while Ni_3Sn reveals near-perfect agreement, the disparity becomes greater toward $x = 0$. This raises concerns whether the $D^{-1}(E)$ model fails to accurately estimate the energy-dependent scattering in Ni_3In.

Therefore, in a second step of more advanced theoretical assessment, we performed *ab initio* calculations of the electron-phonon scattering rates in the relaxation time approximation (RTA) using the PHOEBE code [48]. Figure 3(e) displays the energy-dependent carrier lifetimes for electron-phonon scattering in Ni_3In from RTA calculations at 300 K and the $D^{-1}(E)$ model. It is evident that both frameworks predict an abrupt decrease of $\tau(E)$, starting about 0.1 eV above E_F, which is exactly the energy range where the TFB states of Ni_3In overlap with the more dispersive bands; the inset shows a projection of the RTA scattering rates onto the band structure in the relevant energy range. These puzzling findings pose questions as to why the steep edge in $\tau(E)$ does not manifest itself experimentally in a large Seebeck coefficient.

B. Zener quantum tunneling in Ni_3In

To probe the unusual charge transport behavior of Ni_3In, we leveraged the PHOEBE code to perform calculations within the Wigner transport formalism, a general theoretical framework that extends beyond semiclassical Boltzmann transport theory, capturing additional quantum mechanical transport effects by considering the spectral nature of electronic structure. Through these calculations, we demonstrate that extreme interband scattering is indeed at play in this material but is shrouded by an exotic conduction mechanism due to quantum tunneling between Dirac-like bands, unrelated to the FB itself. Finally, we outline strategies to overcome this challenge in Ni_3In and ways to avoid it in other TFB compounds.

The quantum nature of electrons and their interactions with other quasiparticles such as phonons results in spectral broadening of the electronic band structure. This spectral quality allows them to undergo spontaneous vertical transitions from one band into another, creating an

additional contribution to $\sigma(E)$ [Fig. 4(d)] due to the *Zener tunneling* mechanism [49]. Modern computational theory can predict this effect by means of the Wigner transport formalism, which has been well established in thermal transport [50,51], though only a few studies have considered it in a charge transport context [52–54]. Utilizing the Wigner transport equation (WTE), we calculated $S(T)$ and obtain near-perfect agreement with our experimental data [Fig. 4(b)]. Here, electron-phonon scattering is calculated from first principles in the RTA, and Zener tunneling is accounted for as an additional additive transport contribution by the Wigner formalism, from now on referred to as WTE-RTA. The additional conductivity from Zener tunneling derived in the framework of the WTE can be written as

$$\sigma_{\mathrm{Wigner}} = \frac{g_s e^2}{V N_k} \sum_{k,\nu,\nu',\nu\neq\nu'} \frac{f^0_{\nu'}(k) - f^0_{\nu}(k)}{\epsilon_{\nu'}(k) - \epsilon_{\nu}(k)} \times \frac{v^i_{\nu,\nu'}(k) v^{j*}_{\nu',\nu}(k)[\Gamma_{\nu}(k) + \Gamma_{\nu'}(k)]}{4[\epsilon_{\nu'}(k) - \epsilon_{\nu}(k)]^2 + [\Gamma_{\nu}(k) + \Gamma_{\nu'}(k)]^2}, \quad (1)$$

where $g_s = 2$ stands for the spin degeneracy and V for the crystal unit cell volume and N_k represents the number of wave vectors used to integrate the Brillouin zone. Additionally, ν and ν' represent band indices and v and ϵ the electronic band velocities and energies, respectively, and $f^0(k)$ is the Fermi-Dirac distribution function. The electron-phonon scattering rates Γ are obtained at the RTA level. It can be seen that σ_{Wigner} becomes large when

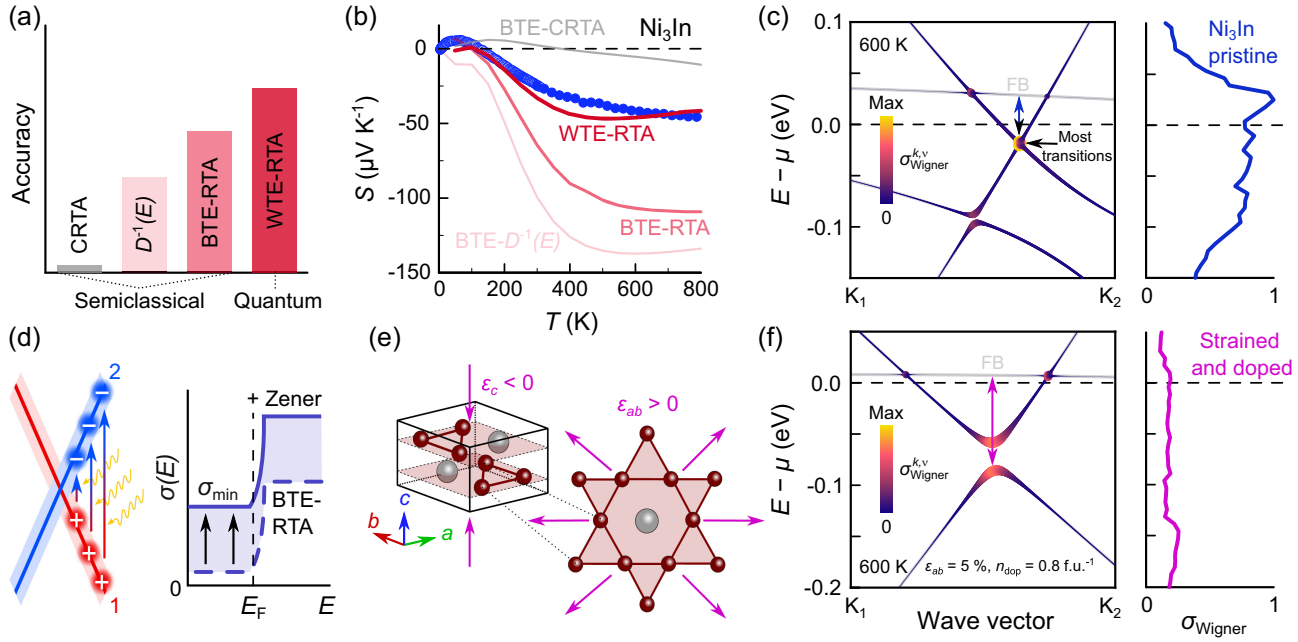

FIG. 4. Zener quantum tunneling transport in Ni_3In. (a) The CRTA framework is the least accurate, as it entirely dismisses any energy dependence of $\tau(E)$. While the latter is approximated within the $D^{-1}(E)$ model and fully included within the RTA framework, the Wigner formalism also takes into account "vertical" interband transitions due to Zener quantum tunneling, as sketched in (d). (b) The experimental data of the Seebeck coefficient $S(T)$ of Ni_3In are compared to various levels of theoretical calculations: BTE-CRTA clearly underestimates S at high T, whereas the BTE-$D^{-1}(E)$ and BTE-RTA results overestimate it. The WTE-RTA formalism yields excellent agreement with experiment. (c) Zener tunneling contribution to electronic transport coming from each high-symmetry band path, as in Eq. (1), without the summation over k and ν, showing that only the Dirac-like bands in Ni_3In with mixed orbital character and strong linewidth overlap around their crossing are relevant. On the right, the associated contribution σ_{Wigner} is plotted (in arbitrary units) for different band fillings. (d) The Wigner term from vertical transitions adds up to the energy-dependent conductivity, yielding a significantly larger σ_{min} compared to the small (suppressed by interband scattering) RTA value and a reduced S compared to the BTE-RTA result. (e),(f) Shifting apart the Dirac crossing from the FB upon strain tuning of Ni_3In enables to switch off the Zener tunneling contribution. As sketched in (e), biaxial tensile strain $\varepsilon_{ab} > 0$ can be realized by compressive strain along the c direction due to a nonzero Poisson ratio. (f) This way, the FB can be decoupled from the Dirac bands in biaxially strained Ni_3In kagome planes, as the former is shifted toward higher energies. This allows switching off Zener tunneling while keeping electron-hole asymmetry, when E_F is adjusted to the FB and away from the Dirac crossing by doping accordingly. For the unstrained and strained plots, the k point ranges are $K_1 = [0.05833, 0.05833, 0]$, $K_2 = [0.10833, 0.10833, 0]$ and $K_1 = [0.04167, 0.04167, 0]$, $K_2 = [0.08333, 0.08333, 0]$ in reciprocal lattice coordinates, respectively.

spectral broadening increases (large Γ) compared to the separation of energy bands and when band velocities are high (dispersive bands).

We observe a significant Zener tunneling transport contribution, σ_{Wigner}, which we note does not exhibit pronounced energy dependence around E_{F} [see Fig. 4(c) right]. In the case of Ni_3In, the additional conductivity decreases the electron-hole transport asymmetry, as indicated in Fig. 4(d), and, thus, reduces $S(T)$. Typically, σ_{Wigner} is much smaller than the conductivity of conventional transport processes taken into account in the Boltzmann transport equation (BTE). However, when several conditions are met—specifically, for bands with large group velocities, small band energy separation, and overlapping linewidths—these transitions can become more pronounced, and in Ni_3In, the Dirac-like bands crossing E_{F} satisfy all these conditions. As shown in Fig. 4(c), Zener tunneling is linked to the Dirac band crossing around E_{F} in Ni_3In.

A natural question arises: How can we overcome this challenge in Ni_3In to realize the high $S(T)$ predicted by the BTE-$D^{-1}(E)$ and BTE-RTA frameworks, and how can we avoid a parasitic contribution σ_{Wigner} in other candidate materials? In $Ni_3In_{1-x}Sn_x$, this could be realized by decoupling the FB from the Dirac bands. The Dirac crossing point has to be pushed above or below E_{F} to restrict the phase space for Zener tunneling. However, this cannot be achieved by mere doping, as the FB needs to be close to E_{F} to provide the necessary interband scattering for a high S. Figures 4(e) and 4(f) show that biaxial strain tuning of the kagome planes can effectively move the FB to higher energy, while the Dirac bands remain completely insensitive, providing the required decoupling. Note that our results agree well with the recent band-structure calculations on strain-tuned Ni_3Sn [55]. Given that the Ni_3In structure type exhibits the capability to accommodate a diverse range of elements and compositions, one can anticipate a considerable level of adjustability in the flat-band states without the need to apply mechanical strain. For example, we suggest that chemical substitution with heavier Pb/Bi atoms instead of In/Sn or substituting Pd/Pt instead of Ni could expand the kagome planes, recovering a high $S(T)$ when the flat bands are decoupled from the Dirac crossing points.

Lastly, we emphasize that, upon evaluating new TE candidate materials, it is probably advisable to avoid Dirac- or Weyl-like crossing points intersecting with the FB, and a slight offset between the two is recommended. Any future study considering the promise of topological TEs should take care to consider this effect, which has also been found theoretically in the topological insulator Bi_2Se_3 [52]. However, Zener tunneling does not necessarily have to be significant. For instance, charge transport in CoSi, where a Dirac point also intersects with a slightly flattened band exactly at E_{F}, can be accurately described using the standard BTE [34,47]. Thus, multiple specific conditions must be met for Zener tunneling to occur, making it a critical, yet ideally rare, obstacle to the design of topological TE materials, in general. In certain band configurations, σ_{Wigner} may even be asymmetric around E_{F} and provide a beneficial effect.

III. CONCLUSION

Frustrated lattice geometries have received enormous attention for hosting exotic correlation phenomena, such as spin-liquid and fractional quantum Hall states. Moreover, destructive interference among electronic hopping paths in such systems can give rise to topological flat bands, which are robust to alloying and disorder. In this study, we unveiled the potential of their electronic structures to drive a large TE effect and experimentally achieved high power factors up to $5\ \mathrm{mW\,m^{-1}\,K^{-2}}$ at room temperature in $Ni_3In_{0.5}Sn_{0.5}$, although an even greater hidden potential is found. Apart from the obvious choice of engineering electronic materials based on the dispersion and bandwidth inherent to the atomic orbitals (s and p orbitals being less localized than d and f orbitals), our work underscores frustrated lattice geometry as another pivotal tuning knob and sheds new light on charge transport in kagome and other flat-band hosting materials. A crucial next step for these intriguing topological and correlated material platforms involves tuning their FBs to E_{F} and understanding their low-energy excitations. Our work uncovers an important new transport mechanism (Zener quantum tunneling), which has previously not been considered in the analyses of these systems. The study of thermoelectricity in TFB compounds comes at the perfect time for several reasons. First, relevant databases and catalogs of FB materials [11,12] have recently been compiled, making it easier than ever to identify the most promising candidates for designing functional materials, such as TEs. Second, the TE field has made substantial progress in modern theoretical calculations of transport properties beyond the constant relaxation time approximation [48,56,57]. These advancements make it more feasible now to study materials with complex carrier scattering, as proposed here.

IV. METHODS

A. Materials synthesis and characterization

High-quality polycrystalline $Ni_3In_{1-x}Sn_x$ samples were synthesized and investigated in two different batches in different laboratories at the National Institute for Materials Science (NIMS) in Tsukuba, Japan and at the TU Wien in Vienna, Austria to confirm the validity and reproducibility of our results. The first batch of $Ni_3In_{1-x}Sn_x$ with $x = 0$, 0.5, 1 was synthesized in a two-step procedure at NIMS: arc melting and consecutive spark plasma sintering. The second batch of samples with $x = 0$, 0.2, 0.4, 0.6, 0.8, 1 was synthesized at TU Wien by first reacting high-purity Ni

and In/Sn bulk metals inside an evacuated quartz tube, followed by induction melting in a water-cooled copper coldboat. Since these compounds do not melt congruently, the resulting ingots were then annealed at 873 K for seven days to obtain phase-pure $Ni_3In_{1-x}Sn_x$. The purity of the used raw elements was 99.99% for Ni and 99.999% for In and Sn. Figure S2 [44] shows that there is excellent reproducibility and agreement between both batches obtained in different laboratories via different techniques.

The structural properties of $Ni_3In_{1-x}Sn_x$ were investigated via x-ray powder diffraction using Cu K-α radiation, which confirmed phase-pure samples and a full solid solution between Ni_3In and Ni_3Sn. Rietveld refinements on the obtained powder diffraction patterns were performed using the programs FULLPROF and POWDERCELL.

B. Property measurements

The electrical resistivity and Seebeck coefficient were measured in the temperature range 300–860 K, using a commercially available setup (ZEM3 by ULVAC/Advance Riko) at TU Wien and at NIMS. Additionally, the low-temperature resistivity of Ni_3In was measured from 4 to 300 K at TU Wien. For this purpose, thin gold wires were spot-welded onto the sample surface and the sample was mounted on a homemade sample probe that was then immersed in a liquid He bath cryostat. Measurements were conducted into the longitudinal direction of the sample (the same direction has been measured at high temperatures) making use of a four-probe method and along the cross section of the sample making use of the van der Pauw method. A comparison between these data is shown in Fig. S3 [44], ruling out any anisotropy in our polycrystalline samples.

The thermal conductivity (see Fig. S1 [44]) was measured at NIMS using a laser flash diffusivity setup by Netzsch. Here, the diffusivity is determined experimentally, and the specific heat is measured simultaneously using a reference sample. The thermal conductivity is then obtained from $\kappa = \alpha c_p \rho_m$ with α being the thermal diffusivity, c_p the specific heat, and d_m the material density. The results of these measurements confirm that electrons dominate thermal transport and that lattice-driven heat transport is insignificant in these metals.

C. Electronic structure calculations

Density functional theory (DFT) calculations of the electronic band structure of pristine Ni_3In [Fig. 2(b)] were performed using QUANTUM ESPRESSO v. 7.1 [58,59], employing optimized norm-conserving Vanderbilt pseudopotentials [60] with a cutoff of 80 Ry on the plane wave expansion and the Perdew-Burke-Ernzerhof exchange-correlation functional [61]. To obtain the ground-state charge density, a uniform $12 \times 12 \times 12$ mesh was employed for integration over the Brillouin zone, with a Methfessel-Paxton smearing of 0.02 Ry. Phonon calculations were performed using density functional perturbation theory [62] on a uniform $4 \times 4 \times 4$ q mesh, and electron-phonon matrix elements were integrated over a $24 \times 24 \times 24$ grid with a Gaussian smearing of 0.015 Ry for the double-delta approximation. Phonon dispersions and density of states were obtained by Fourier interpolation.

Alloy-averaged densities of states of $Ni_3In_{1-x}Sn_x$ [Figs. 2(c) and 2(d)] were calculated by using bulk Green-function methods within the framework of the Kohn-Korringa-Rostoker formalism and the coherent potential approximation (KKR-CPA). This theoretical framework accounts for the disorder due to the alloying or substitution of Sn atoms at the In site.

D. Electronic transport calculations

For transport calculations, DFT calculations were performed using QUANTUM ESPRESSO v. 7.2 [58,59] with the Garrity-Bennett-Rabe-Vanderbilt pseudopotentials [63] parametrized for the Perdew-Burke-Ernzerhof exchange-correlation functional [61] and using a 140 Ry plane-wave coefficient energy cutoff. A $6 \times 6 \times 8$ k mesh and a $3 \times 3 \times 4$ q mesh were used for the initial coarse-grid density functional perturbation theory calculation of the electron-phonon matrix elements. All subsequent transport calculations were performed using the PHOEBE code [48], an open-source package for Boltzmann transport equation solutions. These calculations used the relaxation time approximation (RTA) with the addition of the Wigner transport correction, as well as the constant relaxation time approximation (CRTA) with a 10 fs electron-phonon lifetime as a point of comparison. The BTE-$D^{-1}(E)$ framework utilized the group velocities calculated from the DFT band structures. Instead of multiplication by a constant τ, the energy-dependent relaxation time $\tau(E) \sim D^{-1}(E)$ was multiplied.

The Wigner transport formalism for electrons was calculated as in Ref. [52] using the scattering linewidths determined at the RTA level, where we compute the additive contributions to the Onsager coefficients related to conductivity, $\sigma = L_{EE}$ and the Seebeck coefficient, $S = -[L_{EE}]^{-1} L_{ET}$:

$$\Delta L_{EE} = \frac{g_s e^2}{V N_k} \sum_{k,\nu,\nu',\nu \neq \nu'} \frac{f^0_{\nu'}(k) - f^0_{\nu}(k)}{\epsilon_{\nu'}(k) - \epsilon_{\nu}(k)} \times \frac{v^i_{\nu,\nu'}(k) v^{j*}_{\nu',\nu}(k) [\Gamma_{\nu}(k) + \Gamma_{\nu'}(k)]}{4[\epsilon_{\nu'}(k) - \epsilon_{\nu}(k)]^2 + [\Gamma_{\nu}(k) + \Gamma_{\nu'}(k)]^2}, \tag{2}$$

$$\Delta L_{ET} = -\frac{g_s e^2}{V N_k} \times \sum_{k,\nu,\nu',\nu \neq \nu'} \frac{v^i_{\nu,\nu'}(k) v^{j*}_{\nu',\nu}(k) [\frac{df_{\nu}}{dT} + \frac{df_{\nu'}}{dT}] [\Gamma_{\nu}(k) + \Gamma_{\nu'}(k)]}{4[\epsilon_{\nu'}(k) - \epsilon_{\nu}(k)]^2 + [\Gamma_{\nu}(k) + \Gamma_{\nu'}(k)]^2}, \tag{3}$$

where ν is a band index, Γ is an electron-phonon scattering rate calculated at the RTA level (see Ref. [48] for details), v and ϵ are electronic band velocities and energies, respectively, f is the Fermi-Dirac function, g_s is a spin degeneracy factor, and V is a unit cell volume.

The RTA and Wigner calculations were performed by interpolating the electron and phonon band structures, as well as the electron-phonon matrix elements, to $55 \times 55 \times 75$ k and q meshes. Adaptive Gaussian smearing was used to broaden the delta functions found in the electron-phonon scattering rate expression. To appropriately compare to the polycrystalline sample used in the experimental work, the transport coefficients and the images of the Zener tunneling contribution to transport on bands were plotted as an average over Cartesian directions of the transport tensors.

ACKNOWLEDGMENTS

Research in this paper was financially supported by the Japan Science and Technology Agency (JST) program MIRAI, JPMJMI19A1. The Flatiron Institute is a division of the Simons Foundation. F. G. further acknowledges a Director's Postdoctoral Fellowship through the Laboratory and Directed Research & Development (LDRD) program. The authors also acknowledge the TU Wien Bibliothek for financial support through its Open Access Funding Programme. Furthermore, X. Yan from TU Wien is acknowledged for assistance with Rietveld refinements. G. J. Snyder from Northwestern University, E. S. Toberer from Colorado School of Mines, and J. G. Checkelsky from Massachusetts Institute of Technology are acknowledged for fruitful and stimulating discussions. F. G. and A. P. conceptualized the study. F. G., J. C., A. G., and A. P. analyzed the data and interpreted the results. F. G., together with J. C. and A. P., wrote the initial draft. F. G., M. P., M. G., and S. S. synthesized samples from batch 1 and performed experiments at TU Wien. I. S. synthesized samples from batch 2 and investigated thermoelectric transport at NIMS. F. G. conducted low-temperature measurements. J. C. performed electronic and phonon structure calculations and from there calculated all the electronic transport properties presented in the text. S. D. C. performed DFT calculations of the electronic and phonon structure of pristine Ni_3In and Ni_3Sn. K. P. performed DFT calculations of the electronic structure with and without spin orbit coupling and transport calculations within the CRTA presented in Supplemental Material [44]. S. K. calculated the alloy-averaged densities of states in the KKR-CPA framework. B. W., K. H., T. M., E. B., A. G., and A. P. supervised the work.

[1] Y. Cao, V. Fatemi, S. Fang, K. Watanabe, T. Taniguchi, E. Kaxiras, and P. Jarillo-Herrero, *Unconventional superconductivity in magic-angle graphene superlattices*, Nature (London) **556**, 43 (2018).

[2] J. G. Checkelsky, B. A. Bernevig, P. Coleman, Q. Si, and S. Paschen, *Flat bands, strange metals and the Kondo effect*, Nat. Rev. Mater. **9**, 509 (2024).

[3] B. Sutherland, *Localization of electronic wave functions due to local topology*, Phys. Rev. B **34**, 5208 (1986).

[4] D. L. Bergman, C. Wu, and L. Balents, *Band touching from real-space topology in frustrated hopping models*, Phys. Rev. B **78**, 125104 (2008).

[5] D. Leykam, A. Andreanov, and S. Flach, *Artificial flat band systems: From lattice models to experiments*, Adv. Phys. X **3**, 1473052 (2018).

[6] E. Tang, J.-W. Mei, and X.-G. Wen, *High-temperature fractional quantum Hall states*, Phys. Rev. Lett. **106**, 236802 (2011).

[7] Z. Liu, F. Liu, and Y.-S. Wu, *Exotic electronic states in the world of flat bands: From theory to material*, Chin. Phys. B **23**, 077308 (2014).

[8] L. Ye, M. Kang, J. Liu, F. Von Cube, C. R. Wicker, T. Suzuki, C. Jozwiak, A. Bostwick, E. Rotenberg, D. C. Bell *et al.*, *Massive Dirac fermions in a ferromagnetic kagome metal*, Nature (London) **555**, 638 (2018).

[9] M. Kang, S. Fang, L. Ye, H. C. Po, J. Denlinger, C. Jozwiak, A. Bostwick, E. Rotenberg, E. Kaxiras, J. G. Checkelsky *et al.*, *Topological flat bands in frustrated kagome lattice CoSn*, Nat. Commun. **11**, 4004 (2020).

[10] J. P. Wakefield, M. Kang, P. M. Neves, D. Oh, S. Fang, R. McTigue, S. Frank Zhao, T. N. Lamichhane, A. Chen, S. Lee *et al.*, *Three-dimensional flat bands in pyrochlore metal* $CaNi_2$, Nature (London) **623**, 301 (2023).

[11] N. Regnault, Y. Xu, M.-R. Li, D.-S. Ma, M. Jovanovic, A. Yazdani, S. S. Parkin, C. Felser, L. M. Schoop, N. P. Ong *et al.*, *Catalogue of flat-band stoichiometric materials*, Nature (London) **603**, 824 (2022).

[12] P. M. Neves, J. P. Wakefield, S. Fang, H. Nguyen, L. Ye, and J. G. Checkelsky, *Crystal net catalog of model flat band materials*, npj Comput. Mater. **10**, 39 (2024).

[13] P. F. Rosa and F. Ronning, *A quantum collaboration for flat bands*, Nat. Phys. **20**, 539 (2024).

[14] G. J. Snyder, A. H. Snyder, M. Wood, R. Gurunathan, B. H. Snyder, and C. Niu, *Weighted mobility*, Adv. Mater. **32**, 2001537 (2020).

[15] V. Pecunia, S. R. P. Silva, J. D. Phillips, E. Artegiani, A. Romeo, H. Shim, J. Park, J.-H. Kim, J. S. Yun, and G. C. Welch, *Roadmap on energy harvesting materials*, JPhys Mater. **6**, 042501 (2023).

[16] A. F. Ioffe, L. Stil'Bans, E. Iordanishvili, T. Stavitskaya, A. Gelbtuch, and G. Vineyard, *Semiconductor thermoelements and thermoelectric cooling*, Phys. Today **12**, No. 5, 42 (1959).

[17] A. Zevalkink, D. M. Smiadak, J. L. Blackburn, A. J. Ferguson, M. L. Chabinyc, O. Delaire, J. Wang, K. Kovnir, J. Martin, L. T. Schelhas *et al.*, *A practical field guide to thermoelectrics: Fundamentals, synthesis, and characterization*, Appl. Phys. Rev. **5**, 021303 (2018).

[18] G. J. Snyder and E. S. Toberer, *Complex thermoelectric materials*, Nat. Mater. **7**, 105 (2008).

[19] Q. Yan and M. G. Kanatzidis, *High-performance thermoelectrics and challenges for practical devices*, Nat. Mater. **21**, 503 (2022).

[20] W. Liu, H. S. Kim, Q. Jie, and Z. Ren, *Importance of high power factor in thermoelectric materials for power generation application: A perspective*, Scr. Mater. **111**, 3 (2016).

[21] Y. Pei, X. Shi, A. LaLonde, H. Wang, L. Chen, and G. J. Snyder, *Convergence of electronic bands for high performance bulk thermoelectrics*, Nature (London) **473**, 66 (2011).

[22] M. Zebarjadi, G. Joshi, G. Zhu, B. Yu, A. Minnich, Y. Lan, X. Wang, M. Dresselhaus, Z. Ren, and G. Chen, *Power factor enhancement by modulation doping in bulk nanocomposites*, Nano Lett. **11**, 2225 (2011).

[23] T. Mori, *Novel principles and nanostructuring methods for enhanced thermoelectrics*, Small **13**, 1702013 (2017).

[24] G. Mahan and J. Sofo, *The best thermoelectric*, Proc. Natl. Acad. Sci. U.S.A. **93**, 7436 (1996).

[25] R. S. Whitney, *Most efficient quantum thermoelectric at finite power output*, Phys. Rev. Lett. **112**, 130601 (2014).

[26] J. Maassen, *Limits of thermoelectric performance with a bounded transport distribution*, Phys. Rev. B **104**, 184301 (2021).

[27] J. Park, Y. Xia, V. Ozoliņš, and A. Jain, *Optimal band structure for thermoelectrics with realistic scattering and bands*, npj Comput. Mater. **7**, 43 (2021).

[28] J. Park, *Globally optimal band structure for thermoelectrics in realistic systems*, Phys. Rev. B **106**, 235105 (2022).

[29] S. Ding, X. Chen, Y. Xu, and W. Duan, *The best thermoelectrics revisited in the quantum limit*, npj Comput. Mater. **9**, 189 (2023).

[30] I. T. Witting, T. C. Chasapis, F. Ricci, M. Peters, N. A. Heinz, G. Hautier, and G. J. Snyder, *The thermoelectric properties of bismuth telluride*, Adv. Electron. Mater. **5**, 1800904 (2019).

[31] Y. Pei, A. D. LaLonde, H. Wang, and G. J. Snyder, *Low effective mass leading to high thermoelectric performance*, Energy Environ. Sci. **5**, 7963 (2012).

[32] F. Garmroudi, M. Parzer, A. Riss, C. Bourgès, S. Khmelevskyi, T. Mori, E. Bauer, and A. Pustogow, *High thermoelectric performance in metallic NiAu alloys via interband scattering*, Sci. Adv. **9**, eadj1611 (2023).

[33] C. Li, W. Ren, L. Zhang, K. Ito, and J. Wu, *Effects of Al doping on the thermoelectric performance of CoSi single crystal*, J. Appl. Phys. **98**, 063706 (2005).

[34] D. Pshenay-Severin, Y. Ivanov, and A. Burkov, *The effect of energy-dependent electron scattering on thermoelectric transport in novel topological semimetal CoSi*, J. Phys. Condens. Matter **30**, 475501 (2018).

[35] Y. Xia, J. Park, V. Ozoliņš, and C. Wolverton, *Leveraging electron-phonon interaction to enhance the thermoelectric power factor in graphene-like semimetals*, Phys. Rev. B **100**, 201401(R) (2019).

[36] P. Graziosi, K.-I. Mehnert, R. Dutt, J.-W. G. Bos, and N. Neophytou, *Materials design criteria for ultrahigh thermoelectric power factors in metals*, PRX Energy **3**, 043009 (2024).

[37] M. Y. Toriyama, A. N. Carranco, G. J. Snyder, and P. Gorai, *Material descriptors for thermoelectric performance of narrow-gap semiconductors and semimetals*, Mater. Horiz. **10**, 4256 (2023).

[38] Z. Li, K. Pal, H. Lee, C. Wolverton, and Y. Xia, *Electron-phonon interaction mediated gigantic enhancement of thermoelectric power factor induced by topological phase transition*, Nano Lett. **24**, 5816 (2024).

[39] J. Qiu, S. Zhi, P. Zhao, J. Wang, X. Ma, S. Ye, C. Lin, X. Zhang, Z. Wu, S. Duan *et al.*, *Revealing the significant role of band structure asymmetry on thermoelectric bipolar conduction*, Phys. Rev. B **111**, 045203 (2025).

[40] Q. Yang, S. Yang, P. Qiu, L. Peng, T.-R. Wei, Z. Zhang, X. Shi, and L. Chen, *Flexible thermoelectrics based on ductile semiconductors*, Science **377**, 854 (2022).

[41] P. Zhao, W. Xue, Y. Zhang, S. Zhi, X. Ma, J. Qiu, T. Zhang, S. Ye, H. Mu, J. Cheng *et al.*, *Plasticity in single-crystalline* Mg_3Bi_2 *thermoelectric material*, Nature (London) **631**, 777 (2024).

[42] J. Mao, G. Chen, and Z. Ren, *Thermoelectric cooling materials*, Nat. Mater. **20**, 454 (2021).

[43] L. Ye, S. Fang, M. Kang, J. Kaufmann, Y. Lee, C. John, P. M. Neves, S. F. Zhao, J. Denlinger, C. Jozwiak *et al.*, *Hopping frustration-induced flat band and strange metallicity in a kagome metal*, Nat. Phys. **20**, 610 (2024).

[44] See Supplemental Material at http://link.aps.org/supplemental/10.1103/PhysRevX.15.021054 for additional thermal transport and reproducibility measurements as well as additional computational results on the pristine, undoped compounds.

[45] R. W. McKinney, P. Gorai, V. Stevanović, and E. S. Toberer, *Search for new thermoelectric materials with low Lorenz number*, J. Mater. Chem. A **5**, 17302 (2017).

[46] F. Garmroudi, M. Parzer, A. Riss, A. V. Ruban, S. Khmelevskyi, M. Reticcioli, M. Knopf, H. Michor, A. Pustogow, T. Mori *et al.*, *Anderson transition in stoichiometric* Fe_2VAl*: High thermoelectric performance from impurity bands*, Nat. Commun. **13**, 1 (2022).

[47] Y. Xia, J. Park, F. Zhou, and V. Ozoliņš, *High thermoelectric power factor in intermetallic CoSi arising from energy filtering of electrons by phonon scattering*, Phys. Rev. Appl. **11**, 024017 (2019).

[48] A. Cepellotti, J. Coulter, A. Johansson, N. S. Fedorova, and B. Kozinsky, *PHOEBE: A high-performance framework for solving phonon and electron Boltzmann transport equations*, JPhys Mater. **5**, 035003 (2022).

[49] C. Zener, *A theory of the electrical breakdown of solid dielectrics*, Proc. R. Soc. A **145**, 523 (1934).

[50] M. Simoncelli, N. Marzari, and F. Mauri, *Unified theory of thermal transport in crystals and glasses*, Nat. Phys. **15**, 809 (2019).

[51] M. Simoncelli, N. Marzari, and F. Mauri, *Wigner formulation of thermal transport in solids*, Phys. Rev. X **12**, 041011 (2022).

[52] A. Cepellotti and B. Kozinsky, *Interband tunneling effects on materials transport properties using the first principles Wigner distribution*, Mater. Today Phys. **19**, 100412 (2021).

[53] G. J. Iafrate, V. N. Sokolov, and J. B. Krieger, *Quantum transport and the Wigner distribution function for Bloch electrons in spatially homogeneous electric and magnetic fields*, Phys. Rev. B **96**, 144303 (2017).

[54] G. Kané, M. Lazzeri, and F. Mauri, *Zener tunneling in the electrical transport of quasimetallic carbon nanotubes*, Phys. Rev. B **86**, 155433 (2012).

[55] H. J. Kim, M. J. Kim, J. Lee, J. M. Ok, and C.-J. Kang, *Tuning the flat band with in-plane biaxial strain and the emergence of superconductivity in* Ni_3Sn, Phys. Rev. B **110**, 024504 (2024).

[56] A. M. Ganose, J. Park, A. Faghaninia, R. Woods-Robinson, K. A. Persson, and A. Jain, *Efficient calculation of carrier scattering rates from first principles*, Nat. Commun. **12**, 2222 (2021).

[57] P. Graziosi, Z. Li, and N. Neophytou, *ElecTra code: Full-band electronic transport properties of materials*, Comput. Phys. Commun. **287**, 108670 (2023).

[58] P. Giannozzi, S. Baroni, N. Bonini, M. Calandra, R. Car, C. Cavazzoni, D. Ceresoli, G. L. Chiarotti, M. Cococcioni, I. Dabo *et al.*, *QUANTUM ESPRESSO: A modular and open-source software project for quantum simulations of materials*, J. Phys. Condens. Matter **21**, 395502 (2009).

[59] P. Giannozzi, O. Andreussi, T. Brumme, O. Bunau, M. B. Nardelli, M. Calandra, R. Car, C. Cavazzoni, D. Ceresoli, M. Cococcioni *et al.*, *Advanced capabilities for materials modelling with QUANTUM ESPRESSO*, J. Phys. Condens. Matter **29**, 465901 (2017).

[60] D. R. Hamann, *Optimized norm-conserving Vanderbilt pseudopotentials*, Phys. Rev. B **88**, 085117 (2013).

[61] J. P. Perdew, K. Burke, and M. Ernzerhof, *Generalized gradient approximation made simple*, Phys. Rev. Lett. **77**, 3865 (1996).

[62] S. Baroni, S. De Gironcoli, A. Dal Corso, and P. Giannozzi, *Phonons and related crystal properties from density-functional perturbation theory*, Rev. Mod. Phys. **73**, 515 (2001).

[63] K. F. Garrity, J. W. Bennett, K. M. Rabe, and D. Vanderbilt, *Pseudopotentials for high-throughput DFT calculations*, Comput. Mater. Sci. **81**, 446 (2014).